Internal tide energy transfers induced by mesoscale circulation and topography across the North Atlantic

Adrien Bella[1], **Noé Lahaye** [1], **Gilles Tissot**[1]

[1]INRIA Rennes Bretagne Atlantique & IRMAR – UMR CNRS 6625, Rennes, France

Key Points:

- Advection and shear-internal tides interactions are significant at basin scale, buoyancy interactions are important locally.
- The mesoscale is mainly responsible for a transfer of energy toward smaller internal tide scale.
- Mesoscale induced interactions show an imprint of the spring neap cycle modulated by variations in current positions.

Corresponding author: Adrien Bella, `adrien.bella@inria.fr`

Abstract

The interaction between the internal tide and the mesoscale circulation are studied from the internal tide energy budget perspective. To that end, the modal energy budget of the internal tide is diagnosed using a high resolution numerical simulation covering the North Atlantic. Compared to the topographic contribution, the advection of the internal tide by the background flow and the horizontal and vertical shear are found to be significant at global scale, while the buoyancy contribution is important locally. The advection of the internal tide by mesoscale currents is responsible for a net energy transfer from the large scale to smaller scale internal tide, without significant exchanges with the background flow. On the opposite, the shear of the mesoscale circulation and the buoyancy field are responsible for exchanges between the internal tide and the background flow. The importance of the shear increases in the northernmost part of the domain, and a partial compensation between the buoyancy and the shear contributions is found in some areas of the North Atlantic, such as in the Gulf Stream region. In addition, the temporal variability of the topographic, advection, mesoscale shear and buoyancy gradient induced energy transfers is investigated. The spring neap cycle is the dominant frequency for the topographic scattering, but other frequencies modulate this term in areas of strong mesoscale activity. Mesoscale induced energy fluxes are modulated by both the spring neap cycle and the variation in the mesoscale circulation patterns.

Plain Language Summary

Internal tides are waves generated when the tidal motions, induced by the Moon and Sun gravitational attraction on the ocean, interact with topographical features. Due to the strong variations of water density at various depths, these waves then propagate inside of the ocean interior. Along their propagation, they may interact with ocean currents, and this study aims to investigate the current interactions with the internal tide and their impact on the energy exchanges in the ocean. This analysis is conducted on the North Atlantic basin by the mean of a realistic numerical simulation of high-resolution. The interaction between currents and internal tides is found to primarily transfer energy from large scale waves to smaller ones. This interaction is important for the energy budget of the internal tide at the basin scale. The temporal variability of these current-internal tides interactions shows the same period then the variability of the semi-diurnal astronomical tide. However, these periodic oscillations are modulated by the temporal variability of the currents. The new results of this work should improve our understanding of the internal tide life cycle. This can contribute to a better understanding of the general circulation of the world ocean and therefore of Earth's climate.

1 Introduction

Internal tides are internal waves formed when the barotropic displacement of the water column caused by the tidal potential flows over a topographic feature such as ridges, seamounts or continental slopes. The emitted internal waves can then propagate more than a thousand kilometres for large spatial scale internal tides (Alford et al., 2019), with a decreasing travel distance as this spatial scale decreases. Small scale internal tides dissipate locally. The abundance of topographic features in the ocean, combined with these large propagation distances, make the internal tide an ubiquitous component of the ocean dynamics (Zhao, 2018; Zaron et al., 2022). Moreover, they are a privileged path for astronomical tide energy to fuel the meridional overturning circulation via mixing when they break due to instabilities, producing turbulence (Munk & Wunsch, 1998; de Lavergne et al., 2019, 2020).

This picture is complemented by the presence of mesoscale currents, eddies and density variation across the ocean. In particular, to what extend the interaction between the internal

tide and the mesoscale circulation has an importance on the distribution and dissipation of the internal tide energy remains an open question. This, in turn, has a potential impact on the deep ocean mixing, making the energy interactions between the mesoscale circulation and the internal tide an important object to investigate. Finally, better understanding the dynamics of the internal tide is also important to better predict their sea surface height (SSH) imprint; the internal tide and the mesoscale circulation have the same spatial scale, making the prediction of the mesoscale currents from the SSH without contamination by the internal tide challenging (Ponte & Klein, 2015). This issue is further exacerbated in the context of the recently launched SWOT mission (Ballarotta et al., 2019).

Regional or global numerical simulations (Arbic et al., 2010, 2012; Shriver et al., 2014; Ansong et al., 2017) among others) have helped understanding better the dynamics of the internal tide in a realistic ocean. They have in particular enabled the investigation of the impact of the mesoscale circulation on the propagation of the internal tide. Duda et al. (2018) showed that most internal tide beams crossing a Gulf Stream like jet would be refracted by the current. In an idealised setup, Dunphy & Lamb (2014) investigated the impact of barotropic eddies on the energy flux trajectories of the first baroclinic vertical mode of the internal tide. The mode 1 energy flux was refracted when crossing the eddy. Cold and hot spot of energy flux appeared after the wave had crossed the eddy. The same authors also observed that a baroclinic eddy could transfer energy from low to higher internal tide modes. Furthermore, Kelly & Lermusiaux (2016) and Pan et al. (2021) have studied the impact of the mesoscale on the energy flux divergence of the first internal tide mode in the vicinity of the Gulf Stream and the Palau Islands. Their work reveals a significant mesoscale imprint in the internal tide energy budget. Kelly & Lermusiaux (2016) also showed that a shelf break front is able to modulate the rate of generation of the internal tide by up to 10-20%. Savage et al. (2020) showed in the Tasman sea that the intensity of the energy transfer induced by the advection of the internal tide by the background flow between the vertical mode 1 and 2 is dependent on the scale of the background flow. The background flow was also found to have more importance on higher internal tide modes. All together, these studies show that the mesoscale circulation has an importance on the propagation and the energy budget of the internal tide. However, a quantitative analysis of the impact of the mesoscale flow on the internal tide energy budget, in comparison with other processes affecting its dynamics, has not yet been conducted at the scale of an entire basin.

In this paper, we analyse the internal tide energy life cycle at the scale of the North Atlantic Ocean based on a realistic high-resolution numerical simulation. The different contributions of the energy budget of the internal tide, and in particular the interaction between the internal tide and the mesoscale circulation, are diagnosed and quantified. To this end, a vertical mode decomposition is performed on the hourly outputs of the numerical simulation over a time period of eight month. Such method, which was previously applied by Kelly et al. (2016); Kelly & Lermusiaux (2016); Pan et al. (2021) – among others, allows us to obtain and diagnose the modal energy budget of the semi-diurnal internal tide including in particular the transfers of energy amongst the different vertical modes – which are associated with different length scales.

This paper is organised as follows: Section 2 presents a derivation of the modal energy budget of the internal tide. The numerical simulation used to compute the modal energy budget contributions and the processing of its output are then discussed in Section 3. Section 4 presents the temporal mean of the modal energy budget over the considered domain, its temporal variability and a regional analysis. Section 5 concludes this study.

2 Internal tide governing equations and modal decomposition

2.1 Primitive equations

Similarly to several previous studies (Kelly & Lermusiaux (2016), Pan et al. (2021) among others), a vertical mode decomposition is employed to analyse the energetics of the internal tides. The starting point are the primitive equations under the Boussinesq and hydrostatic approximations with the addition of a tidal potential:

$$\partial_t \boldsymbol{u}_h + (\boldsymbol{u}\cdot\boldsymbol{\nabla})\boldsymbol{u}_h + f\boldsymbol{e_z}\wedge\boldsymbol{u}_h = -\boldsymbol{\nabla}_h p - \boldsymbol{\nabla}_h \Pi_{\text{tide}}, \tag{1a}$$

$$\partial_z p - b = 0, \tag{1b}$$

$$\partial_t b + \boldsymbol{u}\cdot\boldsymbol{\nabla} b = 0, \tag{1c}$$

$$\boldsymbol{\nabla}\cdot\boldsymbol{u} = 0, \tag{1d}$$

with $\boldsymbol{u}(x,y,z,t) = (u,v,w)^T$ the three-dimensional velocity, $\boldsymbol{u}_h$ the horizontal component of $\boldsymbol{u}$, $f(y)$ the Coriolis parameter, $p(x,y,z,t)$ the hydrostatic pressure divided by ρ_0 the reference density, $\Pi_{\text{tide}}(x,y,t)$ the astronomical tidal potential, $b(x,y,z,t)$ the buoyancy and $\boldsymbol{\nabla}_h = (\partial_x, \partial_y)^T$. The Coriolis term is written here formally, and has to be understood as $f\boldsymbol{e_z}\wedge\boldsymbol{u}_h = f(-v,u)^T$. The vertical domain considered extends from the bottom of the ocean to the temporal average of the free surface.

Following Kelly & Lermusiaux (2016), physical fields described by a variable X are decomposed into a slowly varying part and a fast oscillating part describing waves: $X = \overline{X} + \widetilde{X}$. More precisely, the fast varying part in this study is the semi diurnal tidal signal. Furthermore, the slowly varying part of the buoyancy and stratification $N(x,y,z,t)$ (the Brunt-Väisälä frequency) are decomposed into a stationary part, noted B_s, N_s, and a slowly varying part, noted $B^{'}, N^{'}$.

The system (1) is then time-averaged over a few tidal periods, such that the slowly varying part remains approximately constant, but the fast oscillating internal tides vanishes. The result of this procedure is subtracted to (1) and then linearised around the balanced part, considering its amplitude large compared to the small fast waves component. This procedure yields the following equations describing the propagation of internal tides in a realistic ocean:

$$\partial_t \widetilde{\boldsymbol{u}}_h + (\overline{\boldsymbol{U}}\cdot\boldsymbol{\nabla})\widetilde{\boldsymbol{u}}_h + (\widetilde{\boldsymbol{u}}\cdot\boldsymbol{\nabla})\overline{\boldsymbol{U}_h} + f\boldsymbol{e_z}\wedge\widetilde{\boldsymbol{u}}_h = -\boldsymbol{\nabla}_h\widetilde{p} - \boldsymbol{\nabla}_h\Pi_{\text{tide}} \tag{2a}$$

$$\partial_z\widetilde{p} - \widetilde{b} = 0, \tag{2b}$$

$$\partial_t\widetilde{b} + \overline{\boldsymbol{U}}\cdot\boldsymbol{\nabla}\widetilde{b} + \widetilde{\boldsymbol{u}}_h\cdot\boldsymbol{\nabla}_h(B_s + B^{'}) + \widetilde{w}(N_s^2 + N'^2) = 0, \tag{2c}$$

$$\boldsymbol{\nabla}\cdot\widetilde{\boldsymbol{u}} = 0. \tag{2d}$$

The system (2) is complemented by boundary conditions representative of a free surface and a free slip at the bottom:

$$\widetilde{p}(\overline{\eta}_s) = g\widetilde{\eta}, \tag{3a}$$

$$\widetilde{w}(\overline{\eta}_s) = \partial_t(\widetilde{\eta}) + \overline{\boldsymbol{U}}_h(\overline{\eta}_s)\cdot\boldsymbol{\nabla}_h\widetilde{\eta}, \tag{3b}$$

$$\overline{W}(-H) = -\overline{\boldsymbol{U}}_h(-H)\cdot\boldsymbol{\nabla}H, \tag{3c}$$

$$\widetilde{w}(-H) = -\widetilde{\boldsymbol{u}}_h(-H)\cdot\boldsymbol{\nabla}H, \tag{3d}$$

with $\overline{\eta}_s$ the time-averaged sea surface height (SSH) and $\widetilde{\eta}$ the associated fluctuation. For the sake of clarity, overbar $\overline{\cdot}$ and tilde $\widetilde{\cdot}$ will be omitted in the following.

2.2 Vertical modes

At each horizontal position, a set of orthogonal vertical modes is used to project the linearised primitive equations. It provides a clear separation between the barotropic surface

tide and the baroclinic internal tide. Expressing the diagnostics in this basis also allows us to drastically reduce the computational costs associated with high resolution three-dimensional primitive equation simulations over large domains. The modes used in this study are defined with a free surface, similarly as the modes considered in Kelly (2016).

The vertical modes are obtained from the primitive equations with a linearised internal wave propagating inside an ocean devoid of background currents and featuring a temporally averaged stratification profile $N_s^2(x, y, z)$. A plane wave with vertically variable amplitude propagating in the horizontal direction in Fourier space is considered. The equations (2d) are expressed horizontally and temporally in the Fourier domain and subsequently reduced to one equation, leading to a Sturm–Liouville problem whose solutions are the vertical modes Φ_n:

$$\partial_z \left(\frac{\partial_z \Phi_n}{N_s^2} \right) + \frac{\Phi_n}{c_n^2} = 0, \tag{4}$$

where c_n^2 is the eigenvalue of mode n. The basis of modes $\Phi_n(z; x, y)$ is representative of horizontal velocities u and v, and the pressure p. In order to span the vertical velocity w, another basis φ_n is also considered. The two vertical modes bases are linked together by the following relations:

$$\partial_z \varphi_n = \Phi_n, \ \partial_z \Phi_n = -\frac{N_s^2}{c_n^2} \varphi_n. \tag{5}$$

These modes obey the impermeable free slip flat bottom and free surface boundary conditions:

$$\partial_z \Phi_n = 0 \text{ at } z = -H, \quad \text{and} \quad g \partial_z \Phi_n + N_s^2 \Phi_n = 0 \text{ at } z = \eta_s. \tag{6}$$

Last, the vertical modes follow the orthogonality conditions:

$$\int_{-H}^{\overline{\eta}} \Phi_m \Phi_n \, \mathrm{d}z = \int_{-H}^{\overline{\eta}} \frac{N_s^2}{c_n^2} \varphi_m \varphi_n \, \mathrm{d}z + \frac{g}{c_n^2} \varphi_m(\eta_s) \varphi_n(\eta_s) = H \delta_{mn}. \tag{7}$$

Physical fields can be projected onto these two bases following:

$$[u_n, v_n, p_n] = \langle [u, v, p], \Phi_n \rangle \, , \tag{8a}$$

$$w_n = \frac{1}{c_n^2} \left(\langle \varphi_n, w N_s^2 \rangle + \frac{g}{H} w(\eta_s) \varphi_n(\eta_s) \right), \tag{8b}$$

$$b_n = \frac{1}{c_n^2} \left(\langle \varphi_n, b \rangle + \frac{g}{H} \frac{b(\eta_s)}{N_s^2(\eta_s)} \varphi_n(\eta_s) \right), \tag{8c}$$

with $\langle f, g \rangle = \frac{1}{H} \int_{-H}^{\overline{\eta}} f(z) g(z) \, \mathrm{d}z$. They can be reconstructed as follows:

$$[u, v, p] = \sum_n [u_n, v_n, p_n] \Phi_n, \tag{9a}$$

$$[w, b] = \sum_n [w_n, N_s^2 b_n] \varphi_n. \tag{9b}$$

The mode 0 is depth invariant (not shown) and is associated with the barotropic astronomical tide, while the higher modes describe the internal tide. In this study, the modes from 0 to 10 will be considered. Such truncation may lead to unaccounted energy transfers toward higher modes which must be kept in mind when analysing the results.

2.3 Coupled shallow water (CSW) equations and energy budget

The derivation of the modal energy budget is the same as in Kelly et al. (2016), with the addition of the free surface, which leads to an upper boundary term similarly as in Kelly (2016). For this reason, only a sketch of the derivation is presented in this section.

The primitives equations (2) are projected onto the vertical modes defined in equation (4). The horizontal motion and continuity equations are projected onto Φ_m, while the hydrostatic equilibrium and the buoyancy equations are projected onto φ_m. The orthogonality conditions, Leibniz formula for integration and the boundary conditions are then applied on the continuity equation. Finally, the buoyancy is reexpressed in function of the pressure anomaly in the buoyancy equation using the hydrostatic equilibrium, leading to the Coupled Shallow Water (CSW) equations:

$$\begin{aligned}\partial_t \boldsymbol{u}_{h_m} + f\boldsymbol{e_z}\wedge\boldsymbol{u}_{h_m} = &-\boldsymbol{\nabla}_h p_m - \sum_n (\boldsymbol{U}_{mn}\cdot\boldsymbol{\nabla})\boldsymbol{u}_{h_n} - \sum_n \boldsymbol{u}_{h_n} U^{\Phi}_{mn} - \sum_n \mathbf{U}^{\nabla}_{mn}\boldsymbol{u}_{h_n} \\ &- \sum_n w_n \boldsymbol{U}^{z}_{mn} - \sum_n p_n \boldsymbol{T}_{mn} - \frac{1}{H}(\varphi_m(\eta_s)-\varphi_m(-H))\boldsymbol{\nabla}\Pi_{\text{tide}}, \quad (10a)\\ \partial_t p_m - c_m^2 w_m = &-\frac{g}{H}\varphi_m(\eta_s)\boldsymbol{U}_h(\eta_s)\cdot\boldsymbol{\nabla}\eta - \sum_n \boldsymbol{U}^{p}_{mn}\cdot\boldsymbol{\nabla}p_n \\ &- \sum_n p_n \left\langle \varphi_m, \boldsymbol{U}\cdot\boldsymbol{\nabla}\left(\frac{N_s^2}{c_n^2}\varphi_n\right)\right\rangle \\ &+ \sum_n \boldsymbol{u}_{h_n}\cdot(\boldsymbol{B}_{mn}+\boldsymbol{B}^s_{mn}) + \sum_n w_n \left\langle \varphi_m, \varphi_n N'^2\right\rangle, \quad (10b)\\ \boldsymbol{\nabla}_h\cdot(H\boldsymbol{u}_{h_m}) + Hw_m = &\, H\sum_n \boldsymbol{u}_{h_n}\cdot\boldsymbol{T}_{mn}, \quad (10c)\end{aligned}$$

with

$$\begin{aligned}&\boldsymbol{T}_{mn} = \langle \Phi_m, \boldsymbol{\nabla}_h\Phi_n\rangle, && \boldsymbol{U}_{mn} = \langle \Phi_m, \boldsymbol{U}_h\Phi_n\rangle, && U^{\Phi}_{mn} = \langle \Phi_m, \boldsymbol{U}_h\cdot\boldsymbol{\nabla}_h\Phi_n\rangle,\\ &\left(\mathbf{U}^{\nabla}_{mn}\right)_{ij} = \left\langle \Phi_m, \Phi_n\frac{\partial U_i}{\partial x_j}\right\rangle, && \boldsymbol{U}^{z}_{mn} = \langle \Phi_m, \varphi_n\partial_z\boldsymbol{U}_h\rangle, && \boldsymbol{U}^{p}_{mn} = \left\langle \varphi_m, \boldsymbol{U}\frac{N_s^2}{c_n^2}\varphi_n\right\rangle,\\ &\boldsymbol{B}_{mn} = \left\langle \varphi_m, \Phi_n\boldsymbol{\nabla}_h B'\right\rangle, && \boldsymbol{B}^s_{mn} = \langle \varphi_m, \Phi_n\boldsymbol{\nabla}_h B_s\rangle.\end{aligned}$$

This system differs from previous works on three points that are explained here.

First, the buoyancy terms in equation (10b) are equivalent to the buoyancy term in Kelly & Lermusiaux (2016). However, a decomposition between stationary and variable part for the buoyancy was performed in order to limit computational costs, since the variable contribution B is negligible to the modal energy budget (not shown here).

Secondly, generalising the work of Kelly (2016) by considering a free surface leads to the additional contribution $\frac{g}{H}\varphi_m(\eta_s)\boldsymbol{U}_h(\eta_s)\cdot\boldsymbol{\nabla}\eta$. It results in an imperfect compensation of all free surface contributions during the derivation of equation (10b).

Last, the variable stratification term in equation (10b) is not documented in the literature to our knowledge. It appears when the stratification is decomposed into a stationary and variable part: while $\int_{-H}^{\overline{\eta}} wN_s^2\varphi_m \mathrm{d}z$ is reduced by applying the orthogonality conditions, the term $\int_{-H}^{\overline{\eta}} wN'^2\varphi_m \mathrm{d}z$ remains. It compensates the fact that the stationary stratification profile is not fully representative of the instantaneous ocean.

The modal energy budget is obtained by summing the inner product between $\boldsymbol{u}_{h_m}$ and the horizontal motion equation (10a) with the buoyancy equation (10b) multiplied by p_m – where the continuity equation (10c) is used to express w_m as a function of $\boldsymbol{u}_{h_m}$. The result of these operations is the modal energy budget of a given mode interacting with various physical features such as topography or mesoscale flow:

$$\begin{aligned}\overbrace{\partial_t\frac{\boldsymbol{u}_{h_m}^2}{2} + \partial_t\frac{p_m^2}{2c_m^2}}^{\text{temporal variation of energy}} + \overbrace{\frac{1}{H}\boldsymbol{\nabla}_h\cdot(H\boldsymbol{u}_{h_m}p_m)}^{\text{divergence of energy flux}} = &\sum_n (A_{mn}+H_{mn}+V_{mn}+C_{mn}+B^o_{mn}+B^{os}_{mn}\\ &S_{mn}+N^s_{mn}+N_{mn}) - \overbrace{\boldsymbol{\nabla}(\Pi_{tide})(\varphi_m(\eta_s)-\varphi_m(-H))\cdot\boldsymbol{u}_{h_m}}^{\text{Tidal forcing}}, \quad (11)\end{aligned}$$

with

$$A_{mn} = -\left((\boldsymbol{U}_{mn}\cdot\boldsymbol{\nabla})\boldsymbol{u}_{h_n}\right)\cdot\boldsymbol{u}_{h_m} + U^{\Phi}_{mn}\boldsymbol{u}_{h_n}\cdot\boldsymbol{u}_{h_m} - \frac{p_m}{c_m^2}\boldsymbol{U}^{p}_{mn}\cdot\boldsymbol{\nabla}p_n,$$

$$H_{mn} = -(\mathbf{U}^{\nabla}_{mn}\boldsymbol{u}_{h_n})\cdot\boldsymbol{u}_{h_m}, \qquad V_{mn} = -w_n\boldsymbol{U}^{z}_{mn}\cdot\boldsymbol{u}_{h_m},$$

$$C_{mn} = p_m\boldsymbol{u}_{h_n}\cdot\boldsymbol{T}_{nm} - p_n\boldsymbol{T}_{mn}\cdot\boldsymbol{u}_{h_m}, \qquad S_{mn} = -\frac{p_m}{Hc_m^2}g\varphi_m(\eta_s)(\boldsymbol{U}_h(\eta_s)\cdot\boldsymbol{\nabla})\eta,$$

$$B^{o}_{mn} = \frac{p_m}{c_m^2}\boldsymbol{u}_{h_n}\cdot\boldsymbol{\nabla}_h B_{mn}, \qquad B^{os}_{mn} = \frac{p_m}{c_m^2}\boldsymbol{u}_{h_n}\cdot\boldsymbol{\nabla}_h B^{s}_{mn},$$

$$N^{s}_{mn} = -\frac{p_m}{Hc_m^2}p_n\int_{-H}^{\overline{\eta}}\varphi_m\boldsymbol{U}\cdot\boldsymbol{\nabla}\left(\frac{N_s^2}{c_n^2}\varphi_n\right)\,\mathrm{d}z, \qquad N_{mn} = -\frac{p_m}{Hc_m^2}w_n\int_{-H}^{\overline{\eta}}N'^2\varphi_n\varphi_m\,\mathrm{d}z.$$

The first term in the left hand side of equation (11) contains the temporal variation of the internal tide energy. The temporal average of this term over a long period compared to the internal tide period vanishes for stationary flows. It is followed by the horizontal energy flux divergence which diagnoses sources and sinks for the internal tide mode. The right hand side of the equation contains all energy fluxes between the internal tide and the mesoscale circulation, buoyancy field and topography, and the tidal forcing, respectively. The latter projects only weakly on the baroclinic modes (not shown here), because it is constant over depth. It will therefore not be examined in this paper. All coupling terms are the sum over the mode index n of matrix of modes pairs at each time step and each grid point, describing energy exchanges between different internal tide modes, as well as energy fluxes between internal tide modes and the mesoscale circulation. These matrices can be decomposed into an anti-symmetric part, describing exchanges of energy between the internal tide modes, and a symmetric part describing exchanges of energy between the internal tide and the background circulation and buoyancy field.

A physical interpretation of each terms is as follows: A_{mn} represents the advection of the internal tide by the background flow. Since the second term of A_{nm} is negligible compared to the others, it will not be considered in this paper and A_{nm} reduces to:

$$A_{nm} \approx -((\boldsymbol{U}_{mn}\cdot\boldsymbol{\nabla})(\boldsymbol{u}_{h_n}))\cdot\boldsymbol{u}_{h_m} - \frac{p_m}{c_m^2}\boldsymbol{U}^{p}_{mn}\cdot\boldsymbol{\nabla}(p_n).$$

H_{mn} represents the effect of the horizontal shear of the background flow. V_{mn} is the effect of the vertical shear of the background flow. C_{mn} is associated with the horizontal gradient of the vertical modes, which is caused by the topography but also by the mean stratification profile. However, the respective contributions of topography and stratification are difficult to quantify, and the separation of the two effects cannot be discussed in this paper. Since the role played by the stratification is very likely to be negligible at most of the locations, we interpret this term as topographic scattering, as in Kelly (2016). B^{o}_{mn} arises due to the horizontal gradient of the slowly varying part of the background buoyancy, while B^{os}_{mn} arises from the horizontal gradient of the stationary part of the background buoyancy. S_{mn} is an interaction between the temporally averaged free surface and the mesoscale circulation. N^{s}_{mn} represents the interaction between the stationary stratification, the internal tide and the mesoscale circulation. Finally, N_{mn} is linked to the variable stratification.

In the following, a particular attention is given to A_{mn}, C_{mn}, H_{mn}, V_{mn} and B^{os}_{mn}. Indeed, after their quantification (Bella et al., 2023), the other terms have been found to be negligible. As a consequence, they are not shown in further analyses.

3 Data and Methods

3.1 Numerical simulation

The modal energy budget (11) is diagnosed in the high-resolution realistic simulation of the North Atlantic Ocean eNATL60 (Brodeau et al., 2020). It is based on the Nucleus

for European Modelling of the Ocean (NEMO) model (see Madec & the NEMO team, 2008). The model solves the primitive equations under the Boussinesq and hydrostatic approximations with an Arakawa C grid and z-coordinate with partial step. The eNATL60 run includes astronomical tidal forcing with the M2, S2, N2, O1 and K1 frequencies. In addition, surface forcing from the 3-hourly ERA-interim (ECMWF) reanalysis is used, which enables the simulation to develop a realistic mesoscale field. The horizontal resolution of the simulation is 1/60° (about 1.5 km in the mid latitudes) and features 300 vertical levels with a thickness starting from less than 1 m at the top of the ocean to 100 m at the bottom. The hourly outputs of the horizontal velocity $\boldsymbol{u}_h$, sea level, temperature and salinity fields are processed.

The domain of the simulation covers the North Atlantic from approximately 5°N to 65°N as well as the Mediterranean and Black Seas. The area considered in this paper encompasses the entire North Atlantic ocean and is displayed in Figure 1. The time periods analysed ranges from July 2009 to February 2010. To gain more insight on the spatial structure of the energy couplings, seven subdomains with important signature of mode 1 energy flux divergence are examined: two are located on the North, around the Labrador sea and the Faeroe Islands, one is located in the Gulf Stream area and features a strong mesoscale activity, with a well defined continental slope. Two others domains featuring continental slope but weak mesoscale circulation are located in the Bay of Biscay and the West Sahara coast. Last, two subdomains are located around Islands and contain seamounts, with a low mesoscale activity: one is centred around the Azores islands, and the other is located in the Caribbean.

3.2 Vertical modes and modal amplitude computation

In order to obtain the vertical normal modes bases, the mean stratification N_s^2 is computed from the time averaged temperature and salinity using the TEOS-10 equation of state. This routine is the same as the one used in the NEMO model. The Sturm-Liouville problem (4) is then discretised and solved on the staggered vertical grid on each horizontal cell, thus defining the two modal bases at the centre (in the horizontal direction) of each cell. The modal amplitudes u_n, v_n and p_n are obtained by projecting the corresponding fields u, v and p onto the vertical modes basis Φ_n, following (8a)-(8c). Since the horizontal grid is staggered, the horizontal velocity is located at the edge of each cell. Then, the basis Φ_n is interpolated before projecting the velocities. Unfortunately, this step induces a loss of orthogonality for the newly interpolated basis. The horizontal velocity modal amplitudes were corrected *a posteriori* using the cross-projection matrix between the interpolated basis and the bases obtained by solving the Sturm-Liouville problem (4) on the u, v-grids. The modal amplitudes of the vertical velocity are then computed using the continuity equation, following the discrete scheme employed in the NEMO code (Madec & the NEMO team, 2008) – see Appendix 2 for details.

Since the modal decomposition is expected to be less relevant in shallow regions (because bottom and wind stresses are not included in the vertical modes definition), a mask is applied to remove all locations shallower than 250 m.

3.3 Importance of $N(z)$ on the basis definition

The definition of the vertical modes Φ_n and φ_n depends on the temporally averaged stratification profile over the eight months of the simulation output. However, since the stratification of the ocean evolves with time (*e.g.* Barbot et al., 2021, in the context of internal tide dynamics), it means that physical fields are projected onto bases that are not perfectly representative of the solution at a given time. Such inconsistency is mainly accounted for by the cross-modal interaction term N_{mn}, which arises due to the inadequacy between the instantaneous stratification profile and the profile considered in the Sturm–Liouville problem. These spurious energy transfers can be viewed as non diagonal terms,

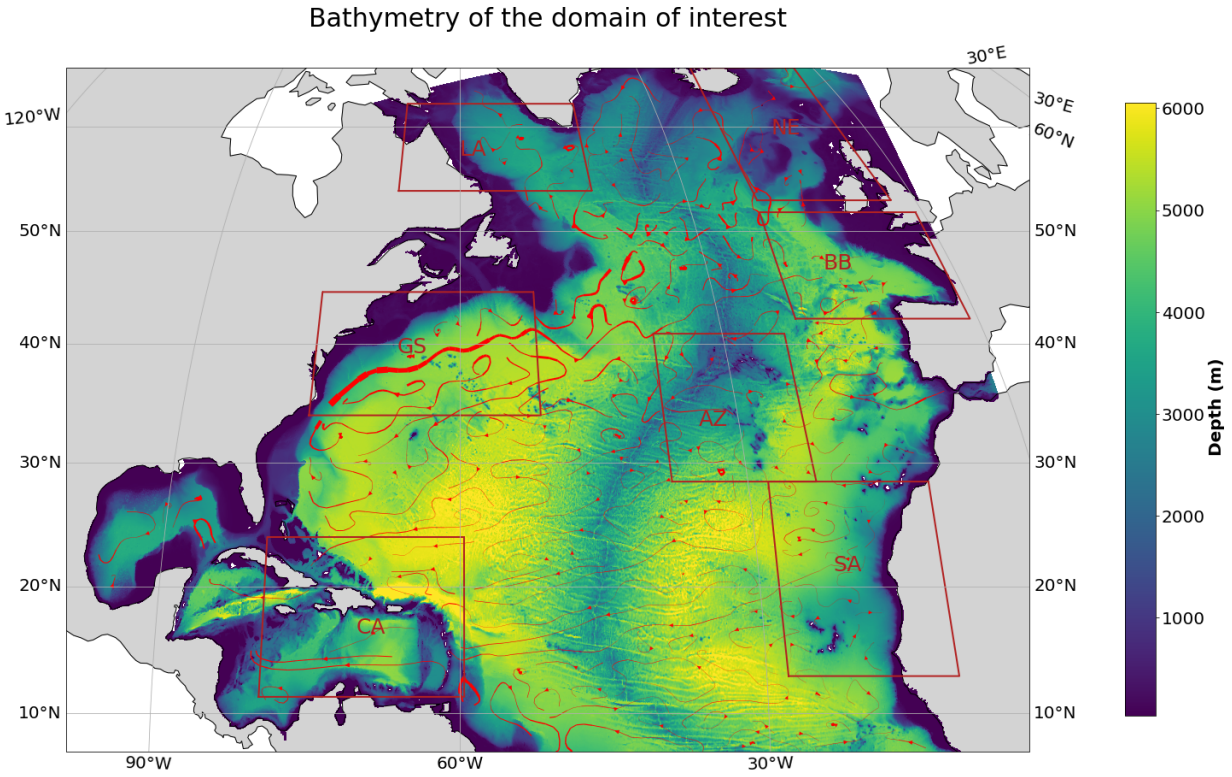

Figure 1: Topography of the eNATL60 domain considered in this paper, colour. Red streamlines: eight months average of the mesoscale circulation at 250 metres depth. The brown boxes highlight the different subdomains considered. Starting from the top right and going clockwise are found the Faroe Islands domain (NE), the Bay of Biscay domain (BB), the Azores domain (AZ), the west Sahara coast (SA), the Caribbean domain (CA), the Gulf Stream domain (GS) and the Labrador domain (LA).

arising because the projection onto the vertical modes bases fails to diagonalise the system. This term would not exist if instantaneous stratification profiles were used.

To mitigate this effect, the energy transfers of equation (11) are computed by performing an *a posteriori* correction to the projection coefficients and vertical modes coupling matrices such as $\boldsymbol{T}_{mn}$. These tensors have been previously computed once with the simulation basis in order to avoid storing their monthly versions, which would require a large storage space. It can be remarked that correcting these tensors is computationally preferable to computing them each month with monthly bases obtained by solving equation (4). After the correction, the magnitude of the term N_{mn} decreases from a significant energy transfer to values that are negligible compared with the dominant terms in the energy budget (11). More details can be found in appendix 1.

3.4 Time filtering

The mesoscale and internal tide signals are obtained by time filtering the horizontal velocities and pressure fields. To reduce the numerical costs associated with the computation of the energy interaction terms of (11), the mesoscale is decomposed on the modal basis as follows:

$$\boldsymbol{U}_h(x,y,z,t) = \sum_n \boldsymbol{U}_{h_n}(x,y,t)\Phi_n(z). \tag{12}$$

The background flow $\boldsymbol{U}_{h_n}$ is obtained from the complete modal velocities amplitudes by using a low-pass filter with a cutoff period of two days. This signal is then substracted to the complete modal amplitude before applying a complex demodulation at a central semi-diurnal frequency $\omega = 1.415 \times 10^{-4}\mathrm{rad\,s^{-1}}$, thus obtaining the internal tide modal amplitudes. The frequency ω corresponds to a period of 12 h 20 min, which is centred between the Solar semi-diurnal component S2 at 12 h and the larger Lunar elliptic semi-diurnal component N2 at 12 h 40 min (Gerkema, 2016). The M2 component is contained in this interval with a period of 12 h 24 min. This choice has been made in order to capture both the M2 and S2 components along with their spectral broadening caused by interaction with the mesoscale flow. Each month is treated separately, with an overlap of 5 days, to reduce numerical costs associated with the time filtering.

The slowly-variable buoyancy field is computed from the daily-averaged temperature and salinity, and the corresponding stratification is then estimated from this buoyancy field as follows:

$$N^{'} = -g\partial_z\left(\frac{\rho-\rho_s}{\rho_0}\right). \tag{13}$$

4 Results

4.1 Time-averaged energy exchanges

We now discuss the diagnostic of the eNATL60 simulation based on the framework of the internal tide vertical mode energy equation (11). We first present the time averaged modal energy budget, analysing the spatial and modal distribution of the dominant energy transfer terms. We then discuss the time-variability of these terms.

4.1.1 Energy flux divergence

The energy flux divergence (see eq. 11) is representative of the sources and sinks for the various modes of the baroclinic tide. Figure 2 shows the energy flux divergence averaged over eight months for modes 1, 2 and 3. For the first mode, main sources are located around prominent seamounts – *e.g.* the Great Meteor chain south of the Azores Islands – and islands, such as Cape Verde. Some continental slopes are also major sites of generation, such as the Bay of Biscay or the US East Coast around 40 ° N. Among these, Cape Verde, the Bay of Biscay continental slope and the Great Meteor Seamounts are also prominent

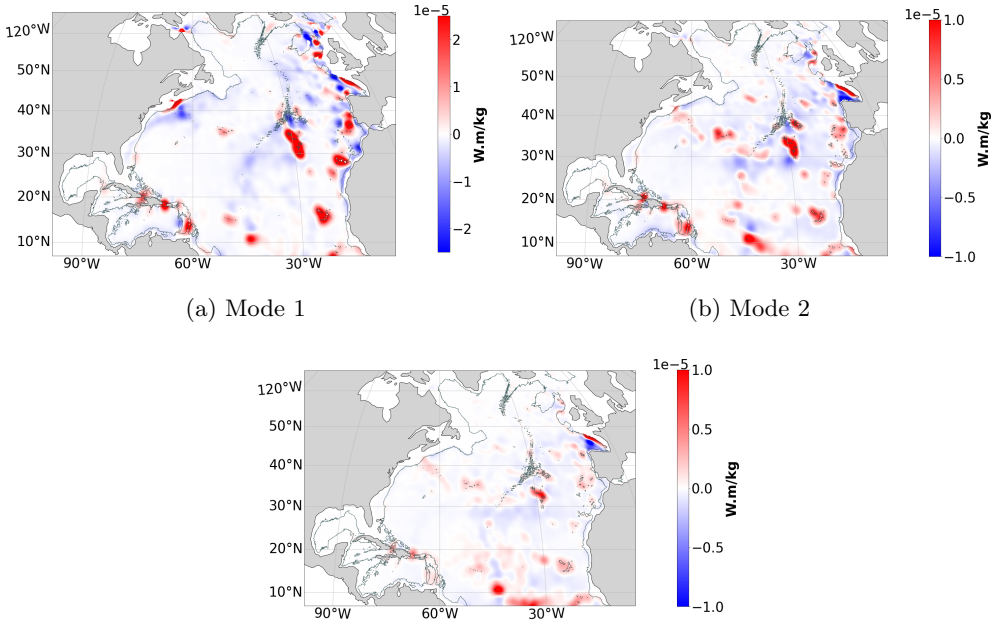

(a) Mode 1

(b) Mode 2

(c) Mode 3

Figure 2: Map of the eight months averaged flux divergence for modes 1 (a) , 2 (b) and 3 (c). A red colour indicates a source of energy for the internal tide mode, a blue spot indicates a sink. A Gaussian filter with a standard deviation of 30 grid points was applied to smooth the divergence field and facilitate interpretations. Gray lines: isobath at 1700 metres depth.

sources for mode 2, while the Bay of Biscay is the most important site of generation for mode 3. Mode 2 and 3 also show a weak source of energy along a beam coming out of the US continental slope.

Main sinks of energy for the mode 1 include continental slopes such as the Western Sahara and along the border of Europe, but also just ashore the US generation site in an area devoid of topography. The imprint of the Gulf Stream is visible in the dissipation pattern of the first baroclinic mode with values as high as values observed along the North Atlantic ridge. A diffuse loss of energy for all modes is located in the eastern part of the Atlantic, especially near the Mid Atlantic ridge. Modes 2 and 3 also show a strong loss of energy in the interior of the bay of Biscay.

4.1.2 Main contributions to the mode 1 internal tide energy budget.

Among all the sources and sinks, the topographic scattering of energy (captured by the C_{mn} term in eq. 11) have attracted the most attention (Lahaye et al., 2020; Buijsman et al., 2020). Figure 3(a) shows the energy exchange between modes 1 and 2 caused by this topographic scattering. Across most of the domain, this process is responsible for a loss of energy for the first mode toward the second, with strong values localised at topographic features. Despite C_{mn} including also the impact of the horizontal variations of stratification, there is no energy exchange in the Gulf Stream area away from topographic features (but with stratification variations), that would suggest a importance of the stratification effects. However, in the north of the domain and at the US continental slope generation site, mode 2 transfers energy toward mode 1. Long term variations (over several months) are observed

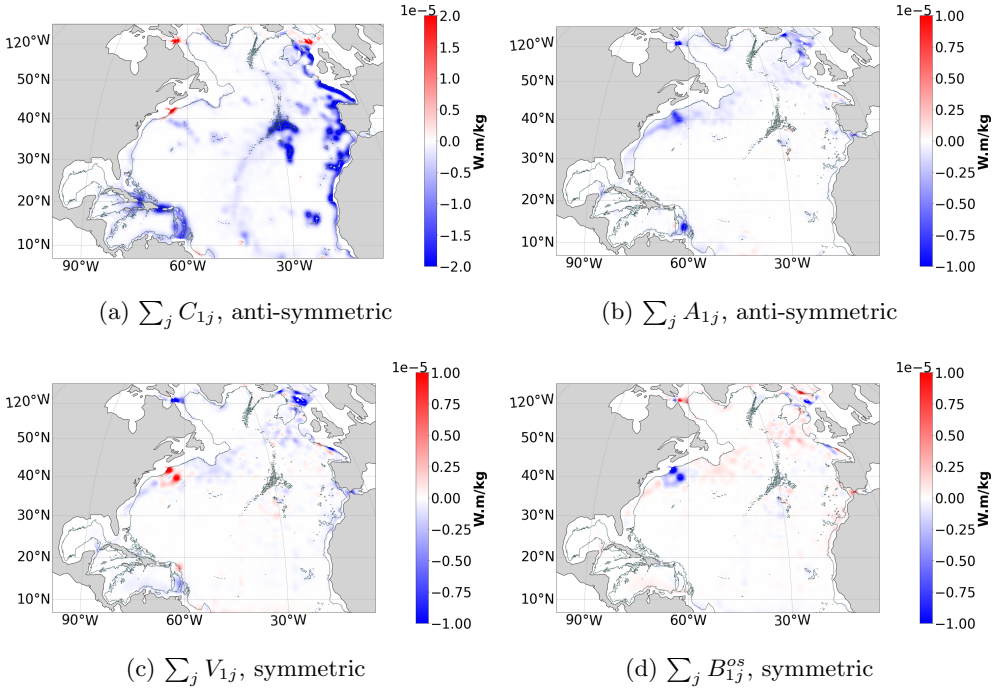

(a) $\sum_j C_{1j}$, anti-symmetric

(b) $\sum_j A_{1j}$, anti-symmetric

(c) $\sum_j V_{1j}$, symmetric

(d) $\sum_j B^{os}_{1j}$, symmetric

Figure 3: Eight months averaged modal energy exchange terms over the North Atlantic for mode 1. (a): anti-symmetric contribution of topographic scattering, (b): anti-symmetric contribution of advection induced energy transfer, (c): symmetric contribution of background flow vertical shear induced energy transfer, (d): symmetric contribution of background buoyancy induced energy transfer. A blue colour indicates a loss of energy, a red colour indicates a gain. The colorbar has different values for the topographic scattering and the mesoscale induced energy transfers. The same smoothing as in Fig. 2 has been applied. Dark grey lines indicate isobath at 1700 metres depth.

in the temporal series of C_{12} integrated over the Gulf Stream domain (*c.f.* section 4.2.1). In addition, some discontinuities are visible in the temporal series of C_{12}, which are associated with the change of monthly averaged stratification used to compute the vertical modes. It might therefore be possible that the variations of stratification is responsible for this sign anomaly at the US Eats coast generation site.

Weaker but noticeable energy transfers between mode 1 and mode 2 caused by the advection of the internal tide by the background flow are visible in areas of enhanced mesoscale activities (Fig. 3b). Similarly to C_{mn}, the advection of the internal tide by the background flow is responsible for an energy transfer from mode 1 to mode 2 across most of the domain. These energy transfers occur in the Gulf Stream, especially in front of the mode 1 US generation site, the Labrador sea and in the vicinity of the Faeroe islands, both near sources of energy for the mode 1. Energy transfers also occur in the Gulf Stream and in the North Atlantic drift, but in a much more diffuse manner. Moreover, A_{12} energy exchange also takes place at the southern part of the Antille arc.

Vertical shear (V_{mn}) and buoyancy (B^{os}_{mn}) induced energy transfers between the mode 1 and the mesoscale/buoyancy field also occur at the western boundary current, the North Atlantic drift and the Northernmost part of the basin (*c.f.* Figure 3, panels c and d). These couplings are of the same magnitude as the advection and change sign across the domain. The buoyancy is a sink of energy for the mode 1 in front of the US generation site. It

is also a sink North of Scotland, and is a source for mode 1 everywhere else. Conversely, the vertical shear interaction is a source in front of the US East Coast slope for the first baroclinic mode, and a sink almost everywhere else. B_{mn} and V_{mn} energy transfers are opposed to each others in the Gulf Stream, the North Atlantic drift and the Labrador sea. This opposition has already been pointed out by Kelly & Lermusiaux (2016) in a idealised simulation including a western boundary-like current and in a regional numerical simulation including the Gulf Stream. In the case of two internal tide modes propagating perpendicularly to a mesoscale current in a thermal wind balance, this compensation can be explained under a few simplifying assumptions – see Appendix 2. However, in eNATL60, this opposition does not hold near the Faeroe islands generation site: the vertical shear induced energy transfer displays strong loss of energy for the mode 1, while the buoyancy term generates weaker sources and sinks of energy for the first baroclinic mode.

4.1.3 Domain integrated modal energy transfers

In order to give a global view of the importance of each kind of energy transfer, we discuss the magnitude of the coupling matrices corresponding to the interaction terms, spatially integrated over the whole domain and temporally averaged over the eight months of the simulation. The following matrices are considered (the other terms of the modal energy budget (11) have been found negligible; see Bella et al. (2023) and Appendix 1 for the N_{mn} term):

- Advection of the internal tide A_{mn}: $-H(\mathbf{U}_{mn}\cdot\boldsymbol{\nabla}\boldsymbol{u}_{h_n})\cdot\boldsymbol{u}_{h_m} - \frac{Hp_m}{c_m^2}\boldsymbol{U}^p_{mn}\cdot\boldsymbol{\nabla}p_n$.
- Scattering by topography and stratification C_{mn}: $Hp_m\boldsymbol{u}_{h_n}\cdot\boldsymbol{T}_{nm} - Hp_n\boldsymbol{T}_{mn}\cdot\boldsymbol{u}_{h_m}$.
- Horizontal shear H_{mn}: $-H(\mathbf{U}^{\nabla}_{mn}\boldsymbol{u}_{h_n})\cdot\boldsymbol{u}_{h_m}$.
- Vertical shear V_{mn}: $-Hw_n\boldsymbol{U}^z_{mn}\cdot\boldsymbol{u}_{h_m}$.
- Buoyancy gradient B^{os}_{mn}: $H\frac{p_m}{Hc_m^2}\boldsymbol{u}_{h_n}\cdot\boldsymbol{B}^s_{mn}$.

These interaction matrices are further decomposed into an anti-symmetric part, representing energy transfers between modes within the internal tide field, and a symmetric part which expresses energy exchanges between the internal tide and the mesoscale circulation/buoyancy field.

Figure 4 shows the above modal energy transfer matrices for the North Atlantic. Basin wide, the topographic scattering C_{mn} is predominant. It is the only term able to transfer efficiently energy to non neighbouring modes. It is exactly anti-symmetric by construction, converting energy from low to high modes on average. The advection term is significant for all baroclinic modes and becomes important starting from mode 2: A_{12} is worth 16% of C_{12} but 8% of $\sum_{i=2}^{10} C_{1i}$ while $\sum_{i=4}^{10} A_{3i}$ is worth 31% of $\sum_{i=4}^{10} C_{3i}$. A_{mn} also has a very weak symmetric part and transfers energy from large to small scale internal tides. This forward cascade of energy has been diagnosed from mooring data south of the Azores Islands by Löb et al. (2020), who found evidences that the mesoscale flow is able to transfer energy from low to high modes. A high value of A_{00} is caused by energy exchanges mainly on continental slope and in areas of topography gradients. This is likely caused by the intensification of the barotropic tide velocities over some continental shelf and their associated high gradient over slopes, increasing $((\boldsymbol{U}_{mn}\cdot\boldsymbol{\nabla}\boldsymbol{u}_{h0})\cdot\boldsymbol{u}_{h0})$ even in a presence of a weak mesoscale flow.

In contrast to A_{mn} and C_{mn}, the vertical and horizontal shear are characterised by their strong symmetric part (Figure 4, panels c and d). The horizontal shear acts as a source at the scale of the basin, having its strongest contribution for the mode 1. For this mode, H_{mn} is as important as the advection term. However, its importance decreases for higher modes, making it non significant compared to the topographic scattering for mode 2 and higher at global scale. On the contrary, the vertical shear acts as a sink for the internal tide when integrated over the domain, although figure d shows V_{mn} acting as a source of energy for the first baroclinic mode. The importance of V_{mn} decreases for higher modes as for the horizontal shear term, and overall shows a smaller intensity than H_{mn} but part of it

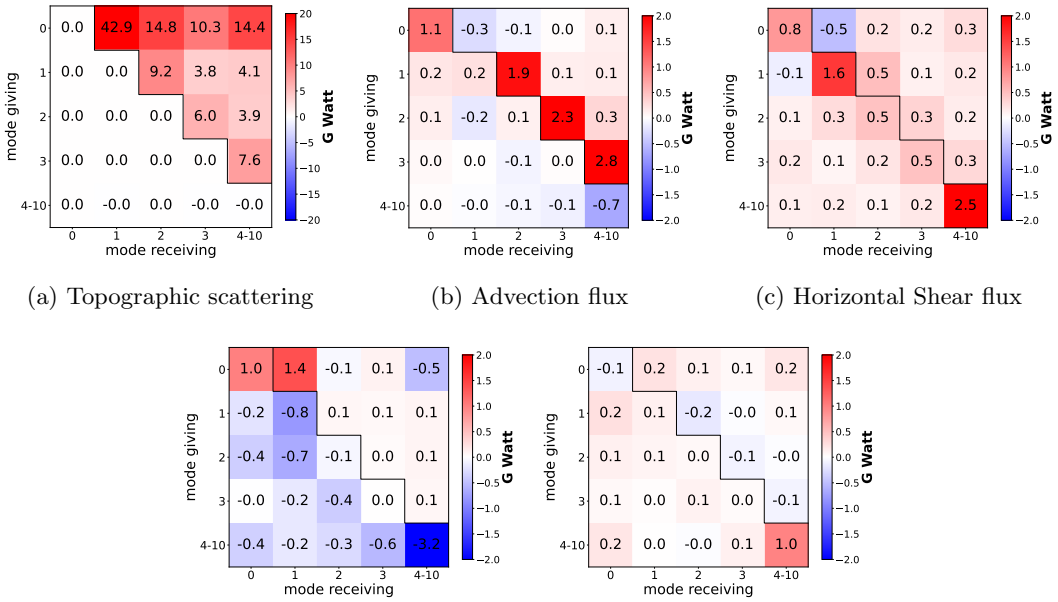

(a) Topographic scattering (b) Advection flux (c) Horizontal Shear flux

(d) Vertical Shear flux (e) Buoyancy flux

Figure 4: Matrices of time-averaged energy couplings integrated over the North Atlantic domain. A positive (resp. negative) value indicates an energy transfer from the row to column mode (reps. column to row). Upper triangle: anti-symmetric part of the energy couplings. Lower triangle and diagonal: symmetric part of the couplings. Modes 4 to 10 are grouped together. Panel a: topographic scattering, b: advection coupling, c: horizontal shear coupling, d: vertical shear coupling, e: buoyancy coupling.

is caused by the compensation between regions of different signs (*c.f.* Figure d). Important values of $\sum_{i=4}^{10}\sum_{j=4}^{10} H_{ij}$ and $\sum_{i=4}^{10}\sum_{j=4}^{10} V_{ij}$ are noticeable, but these are the sum of several interactions, complexifying the interpretation.

Finally, the buoyancy term B^{os}_{mn} (panel e of Figure 4) is weak on average over the domain. However, part of this weakness is due to compensation between regions of different sign. Figure 3 suggests that it is locally important in the energy budget of the first baroclinic mode in the vicinity of the Gulf Stream, the North Atlantic Drift or the northernmost part of the domain. This justifies investigating more closely the regional distribution of these energy transfer terms, which is done in the next section.

4.1.4 Analysis of regional energy budgets

We now present a regional investigation of the modal energy budget (11), based on a spatial integration of the time-averaged coupling matrices over the subdomains defined in section 3. As previously, the energy transfer terms are decomposed in their symmetric and anti-symmetric parts, and the latter is further separated into exchanges with lower and higher modes, before summing the results over the interacting mode n. The barotropic to baroclinic topographic conversion is also isolated. Figure 5 shows the result of this procedure for the first three baroclinic modes.

Among the subdomains, the most energetic internal tide generation are found in the Azores and Faeroe Islands surroundings, while the Gulf Stream and Labrador areas are places of less intense generation. Topographic scattering is the only significant source of modal energy transfer for the first three baroclinic modes for the Azores, West Sahara coast, Caribbean and the Bay of Biscay subdomains. However, for the three remaining subdomains, it is not the dominant contribution of the energy budget. Advection by the background flow is dominant for the modes 2 and 3 in the Gulf Stream, Labrador and Faeroe Islands areas. For these three places, strong symmetric exchanges are the most important transfers observed for the mode 1 energy budget. In the Gulf Stream and Labrador areas, shear and buoyancy cancel each other out, as previously reported by Kelly & Lermusiaux (2016), leaving the advection the dominant resulting coupling. As mentioned previously, this does not hold for the Faeroe islands surrounding. Here the horizontal shear is the prominent cause for energy transfer toward the mesoscale circulation. In the Labrador domain, the shear-induced energy transfers between ITs and the mesoscale circulation have values comparable with the Gulf Stream domain, while the associated eddy kinetic energy (EKE) is one order of magnitude weaker and the IT generation is of similar amplitude. It is well known (*e.g.* Rainville & Pinkel, 2005) that the group velocity of internal waves decreases pole-ward, which could results in such a reinforced mesoscale-IT interaction in the northernmost regions. This may indicate that the high latitudes – at least in the North Atlantic – are a privileged place for internal tide dissipation through wave-mesoscale circulation energy exchange, at the condition that the compensation between vertical shear and buoyancy induced transfers does not hold.

4.1.5 Mode 1 energy budget residual: validation of the modal decomposition

To asses the validity of the modal analysis, the eight months averaged residual of the modal energy budget for mode 1 is plotted in Figure 6b, alongside the divergence of the mode 1 energy flux across the North Atlantic (Figure 6a). This allows to estimate the fraction of the energy flux divergence which is not explained by the five dominant terms considered in the modal energy budget (11), as well as assessing the physical pertinence of the residual.

All sources of energy for the mode 1 present in the divergence are absent in the residual, while most of the residual shows dissipation pattern at topographic features. Part of this

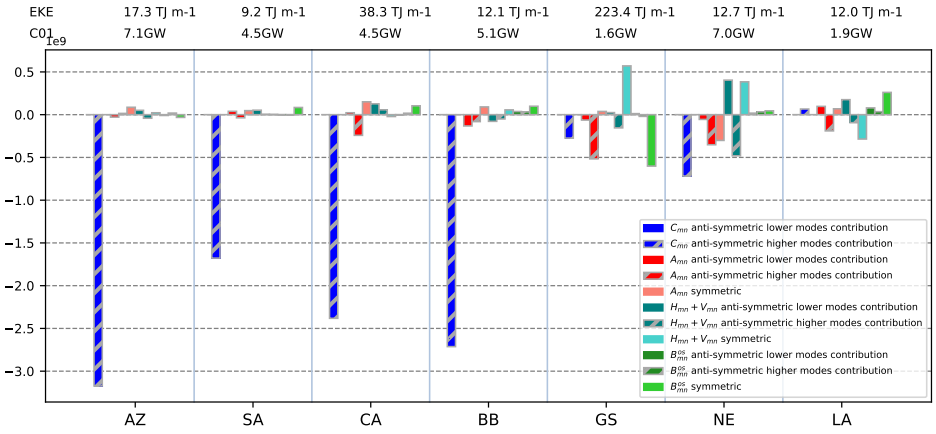

(a) Mode 1

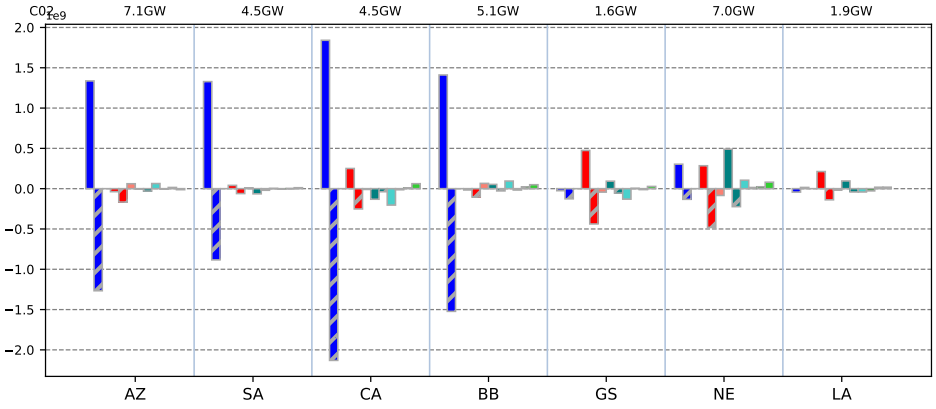

(b) Mode 2

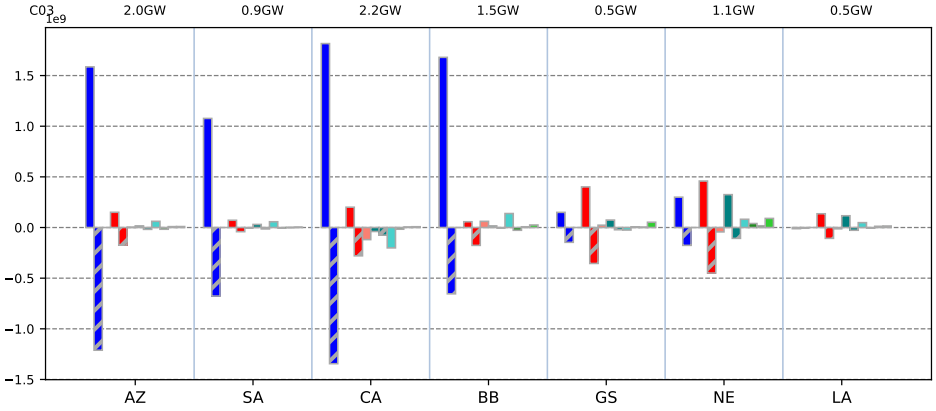

(c) Mode 3

Figure 5: Temporally averaged energy transfers as expressed in equation (11) and integrated over various subdomains for mode 1: a, mode 2: b and mode 3: c. From left to right: Azores, Sahara, Caribbean, Bay of Biscay, Gulf Stream, Nordic Europe and Labrador domains. On top of the Figure: Time-averaged mesoscale kinetic energy at 250 metres depth horizontally integrated over each domain. On top of each plot: time-average of the barotropic tidal conversion integrated over each domain for the mode of interest.

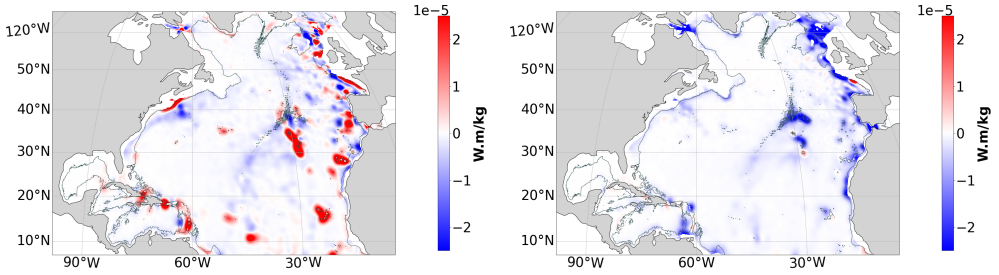

(a) Energy flux divergence

(b) Energy budget residual

Figure 6: a: eight months average of the energy flux divergence for mode 1. b: eight month average of the residual of mode 1 energy budget (energy flux divergence minus all the couplings considered: advection, horizontal shear, vertical shear, topography and steady buoyancy). A blue colour indicates dissipation, a red colour a source of energy. A Gaussian filter with a standard deviation of 40 grid points was applied to both fields to facilitate interpretation. Dark grey line: isobath at 1700 metres depth.

dissipation might be caused by the modal truncation (at $m = 10$), which discards the energy transfers involving the higher modes. This hypothesis is supported by the fact that the dissipation at topographic features occurs at the same places than the C_{12} topographic scattering: the eastern boundary of the Atlantic, the seamounts south of the Azores Islands, the Islands themselves and the North mid Atlantic ridge. However, $C_{1,7-10}$ are negligible when integrated over the domain, suggesting that the topographic scattering coupling the mode 1 to mode higher than 6 is negligible. As mentioned in section 2.3, the parameterised dissipation of the model was not taken into account in our analysis and therefore remains in the residual. In particular, it could account for the important values around the Faeroe Islands where the internal tide does not propagate far form its generation site. It must therefore be locally dissipated, and one way for the mode 1 to loose energy could be an intensified model dissipation. Other terms of the modal energy budget not shown in this paper have been found to be negligible (when evaluated over subdomains and/or over small time periods). They may contribute to the residual, but only weakly. Another factor signing on the residual could be numerical errors made during interpolations and gradients computation, in particular at steep topographic slopes.

Beam like dissipation structures emanating from the Great meteor seamounts south of the Azores could be linked to nonlinear wave-wave interactions, which were not diagnosed in this study. As a final remark, we note that the residual is relatively important in the North, indicating a strong dissipation of mode 1. These regions need closer investigations in the future as they exhibit a strong impact of the mesoscale / internal tides interactions, with an important contribution of the shear-induced energy transfers which differs strongly from other regions such as the Gulf Stream area, as explained previously.

4.2 Temporal variability

We now investigate the time variability of the various energy transfer terms. Two main factors can affect the importance of the energy transfers in equation (11): the variation of the internal tide amplitude and the change in mesoscale currents strength and position. The temporal variations they induce can be decomposed into a part correlated with the astronomical tide – which essentially reflects the spring-neap cycle – and a variability uncorrelated with the astronomical tide.

543 #### *4.2.1 Time variability*

544 The temporal variability of the energy exchanges of (11) is examined first by integrat-
545 ing them spatially over the various sub-domains considered in the present paper. Figure 7
546 shows the resulting temporal series. Discontinuities in the signals at the transition between
547 months are attributed to the change of basis on which the energy terms are expressed.
548 Such discontinuities are particularly visible at the transition between December-January
549 and January-February.

550 In the Azores, the smooth variations of the topographic scattering are strongly corre-
551 lated with the barotropic tide. However, in areas of high mesoscale variability such as the
552 Gulf Stream domain, *c.f.* panel b of Figure 7, additional perturbations are visible and make
553 the energy transfer less correlated with the barotropic tide. Overall, such less correlated
554 signal in areas of high mesoscale activity does not affect the basin-wide high correlation of
555 C_{12} with the barotropic tide, as can be seen in panel c of Figure 7.

556 Likewise, at the basin scale, the spring neap cycle strongly signs on the temporal
557 variability of the advection flux A_{12}, although the latter appears to be modulated – most
558 likely by the mesoscale variability. In contrast, the variability of A_{12} in the Gulf Stream
559 domain (Fig. 7.b) shows almost no imprint of the spring neap cycle visible in the barotropic
560 kinetic energy. Compared to the advection term, both buoyancy and vertical shear induced
561 energy fluxes in the Gulf stream area are modulated by the spring neap cycle, *c.f.* Figure 7b.
562 The spring neap cycle is also visible at global scale for the vertical and horizontal shear
563 terms, as shown in panel c of Figure 7. Such visual correlation between the mesoscale
564 induced energy fluxes and the spring neap cycle integrated over large spatial areas with
565 respect to the mode 1 length wave does not imply that this correlation holds at a local
566 scale, where it is unlikely to exist.

567 #### *4.2.2 Impact of the background flow on the temporal variability of A_{mn}*

568 As mentioned above, the advection-induced transfers exhibit some variability at time
569 scales different from the intrinsic tidal dynamics (spring-neap cycle). We now investigate
570 the evolution of these transfers, in conjunction with modulation of the mesoscale flow, in
571 the Gulf Stream domain in an attempt to clarify in which way the mesoscale variability
572 impacts the variability of the mesoscale-induced energy transfers of equation (11). Similar
573 mechanisms were recently reported off the Amazon shelf by Tchilibou et al. (2022) for the
574 internal tide energy flux.

575 To study the impact of the mesoscale on the variability of the internal tide energy
576 flux, the monthly average of the mode 1 energy flux in the Gulf Stream area is overlaid with
577 the mesoscale circulation at 250 metres depth and the monthly average of A_{12} in Figure 8.
578 Alongside these maps is displayed the monthly average of A_{mn} integrated over the Gulf
579 Stream domain for July, October and February. At the domain scale, the advection energy
580 flux decreases from July to October and from October to February for the modes pairs 1-2,
581 2-3 and 3-4 to 10 (*c.f.* panels b, d and f). In parallel, the monthly average position of the
582 Gulf Stream varies significantly (*c.f.* panels a, c and e). This causes the internal tide beam to
583 interact with different mesoscale patterns over time, leading to different trajectories. These
584 various trajectories are then the cause of variable A_{mn} energy flux pattern (*c.f.* map plots
585 in Figure 8), leading to the decrease of A_{mn} between July and February. In the mean time,
586 the EKE at 250m for the entire domain increases from 234 TJm^{-1} in July to 240 TJm^{-1}
587 in October before decreasing to 210 TJm^{-1} in February. It is therefore unlikely that the
588 variations in the strength of the current is responsible of the decrease of A_{mn} between July
589 and October.

590 The variations in the path of the Gulf Stream are therefore important for the energy
591 budget of the internal tide and are the cause of the non spring-neap cycle variations observed
592 in the Gulf Stream domain for A_{mn} in Figure 7. By construction, A_{mn} exhibits a linear

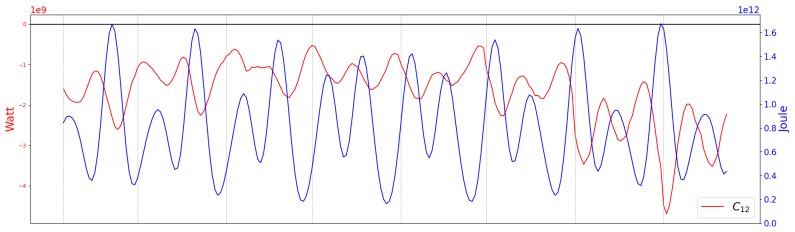

(a) Azores domain

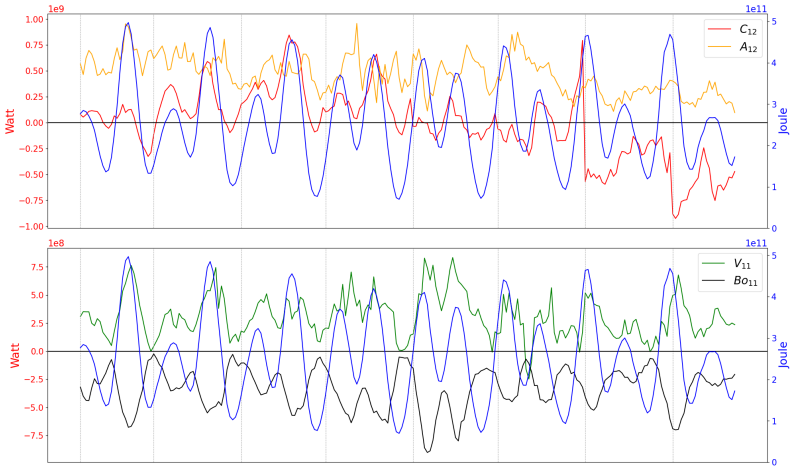

(b) Gulf Stream domain

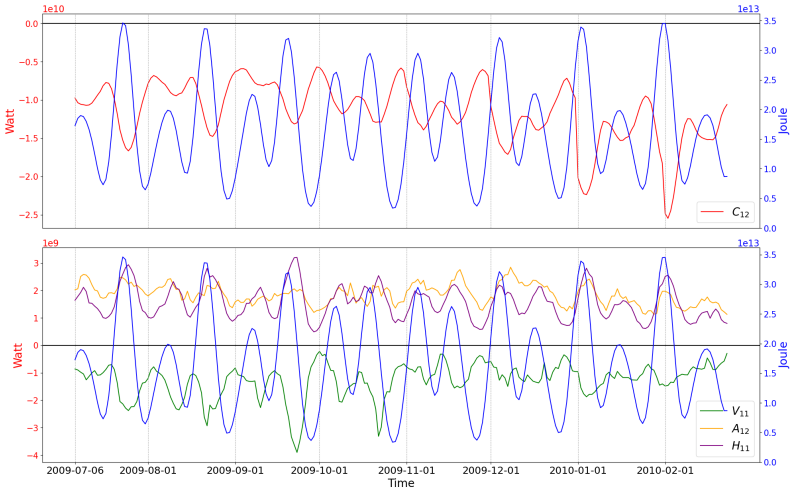

(c) North Atlantic domain

Figure 7: Temporal variation over eight months of the energy transfer between mode 1 and mode 2 or mode 1 and the mesoscale flow/buoyancy field integrated over the Azores domain: panel a, the Gulf Stream domain: panel b, and the North Atlantic: panel c. Panels a, b and c contain the energy transfer caused by the topographic scattering in red, while panels b and c display the energy fluxes caused by the advection of the internal tide by the mesoscale circulation in orange. Moreover, the vertical shear term is plotted in green in panels b and c and the horizontal shear term is plotted in purple in panel c. Last, the buoyancy term B^{os}_{mn} is displayed in black in panel b. A negative value indicates a loss of energy for mode 1 and conversely. The kinetic energy of the barotropic tide integrated over the corresponding domains have been plotted in blue at the corresponding y axis on the right side of the plots.

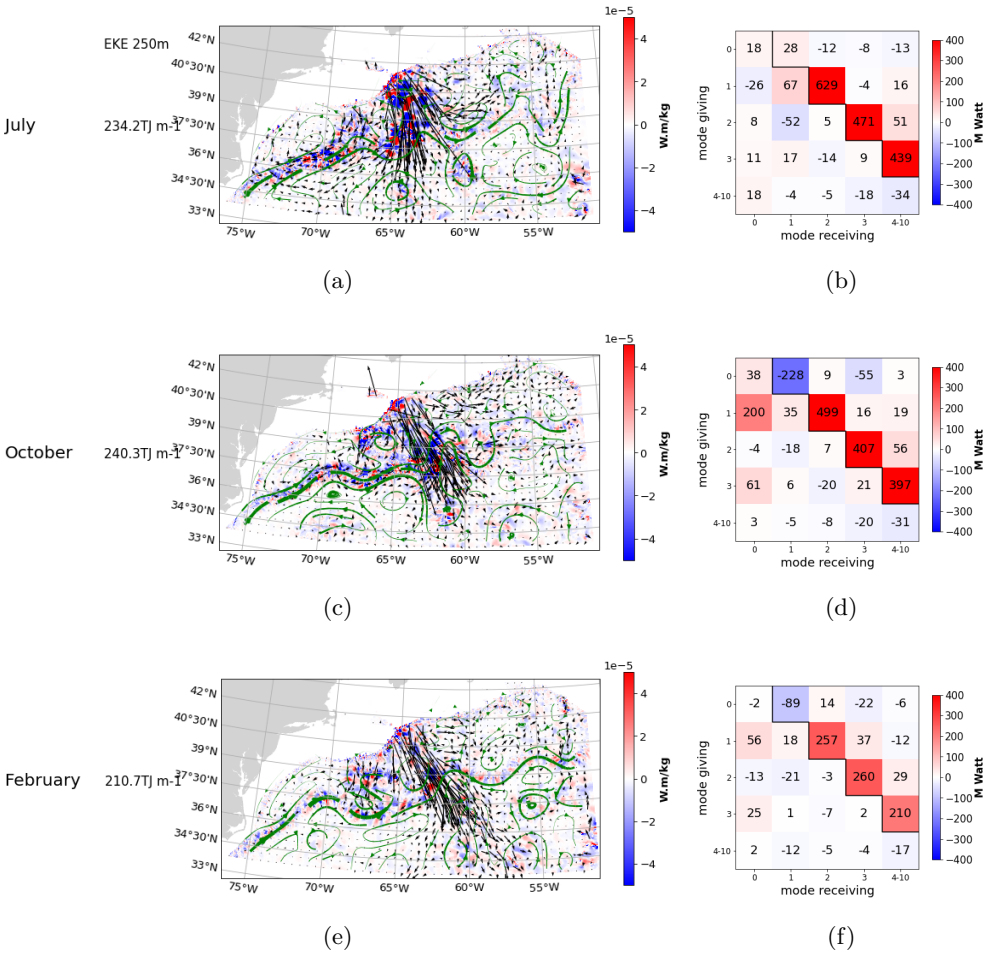

Figure 8: Monthly-averaged advection-induced energy transfers between mode 1 and mode 2 in the Gulf Stream domain. A_{12} for the months of July (a), October (c) and February (e), where negative values indicate a loss of energy for mode 1 and a gain for mode 2. Green streamlines denote the associated mesoscale flow at 250 metres depth, and black arrows the mode 1 energy flux. Dark gray line are isobaths at 1000, 2000 and 3000 metres depth. The integrated mesoscale kinetic energy at 250 m is indicated on the left. The corresponding domain-averaged matrices A_{nm} are shown in panels b, d and f (where the anti-symmetric part is in the upper triangle and the symmetric part in the lower triangle, diagonal included). Sign conventions are identical to Figure 4.

dependency on the amplitude of the mesoscale current, and variations in the amplitude of mesoscale currents can be expected to have an impact on the time variation of the mesoscale induced energy fluxes. In the present case, however, it appears that variations in the strength of the Gulf Stream cannot explain the variability of A_{mn}, which is rather dominated by the configuration of the mesoscale flow.

5 Conclusions

The internal tide energy interactions with the mesoscale circulation, topography and buoyancy field were studied using eight months of a high resolution numerical simulation over the North Atlantic. With the help of a vertical modes decomposition, the modal energy

budget was quantified globally and regionally at seven subdomains with strong internal tide activity.

Among the various energy fluxes highlighted by the modal energy budget (11), the most important one is the topographic scattering, followed by the advection of the internal tide, which is significant for all baroclinic modes and important from mode 2 onward. These two terms transfer energy from the large scale internal tide toward the small scale internal tide without exchange of energy with the mesoscale circulation. On the contrary, the horizontal and vertical shear terms, as well as the buoyancy term, are able to transfer energy between the internal tide and the mesoscale circulation/buoyancy field. In the Gulf Stream area, the north Atlantic drift and the Labrador sea, the vertical shear and buoyancy energy fluxes were found to compensate each other for the first mode. However, this compensation does not appear to hold in the vicinity of the Faeroe islands, the shear contribution being compensated over the subdomain by a locally significant symmetric part of A_{mn}.

The spatial distribution of these energy interactions is strongly heterogeneous: the energy transfers induced by the mesoscale flow are obviously found only in areas with strong mesoscale activity, such as the Gulf Stream and in the North Atlantic drift. However, these couplings are also intensified in the North of the domain – in particular in the Labrador sea and around the Faeroe islands, while these regions exhibit EKE level an order of magnitude smaller than the Gulf Stream area.

The compensation between the vertical shear and buoyancy induced energy fluxes, and the cause of the intensified mesoscale-induced fluxes in the northernmost part of the North Atlantic, deserve further work to clarify the underlying dynamical processes at stake.

The temporal variability of all the couplings discussed in this paper is dominated by the spring neap cycle. This frequency is the strongest for the topographic scattering, although other frequencies appear in the corresponding time series in area of strong mesoscale activity. The spring-neap cycle is also noticeable in the variation of the mesoscale-induced coupling terms, but a significant part of their variation is impacted by others frequencies. For the energy exchanges associated with advection by the mean flow, a detailed investigation of the configurations associated with different magnitudes of the interaction term showed that, in the Gulf Stream area, these non spring-neap cycle variations seem to be more driven by variations of the patterns of the mesoscale currents than by their intensity.

The results of this paper improve our understanding of the internal tide energy lifecycle, with a new light on the internal tide-mesoscale flow energy interactions. In turns, these findings may help to understand the deep water mixing in the ocean, and especially its spatial distribution, which is recognised as being of importance for the meridional overturning circulation (Whalen et al., 2020). In particular, we report that the advection term is able to transfer a significant amount of energy from large scale internal tide to high modes (typically, $m \geq 4$), that do not propagate over long distances and dissipate locally (*e.g.* Vic et al., 2019). However, some technical limitations of our study should be clarified: in particular, the modal decomposition framework we use entails a modal truncation error. Besides, we highlighted that the somewhat arbitrary choice for the stratification associated with the vertical mode definition can lead to a miss-representation of the various energy transfers – which we tried to mitigate using a monthly average. Using a decomposition that more explicitly captures the interaction between low modes and small scale internal waves would be beneficial for a more detailed diagnostics of the IT lifecycle down to (parameterised) mixing. This could be particularly interesting in the regions where mesoscale-internal tide interaction seem to be of importance. Further work could also extend the present analyses to other regions of the ocean – including the Luzon straight in the Pacific, which is known as a strong generation site not far from the Kuroshio path (Pickering et al., 2015) – and investigate interaction terms that were left aside in this study, in particular the nonlinear wave-wave interactions and the modelled dissipation.

1 Importance of basis definition

To compute the terms of equation (11) on monthly bases with physical fields projected on the eight months basis, we correct *a posteriori* each of these fields using the associated transition matrix:

$$P_{nk}(x,y) = \frac{1}{H+\eta_s^m}\int_{-H}^{\eta_s^m} \Phi_k \Phi_n^m \mathrm{d}z, \tag{1a}$$

$$P_{nk}^{-1}(x,y) = \frac{1}{H+\eta_s}\int_{-H}^{\eta_s} \Phi_k \Phi_n^m \mathrm{d}z, \tag{1b}$$

with Φ_n the eight months basis and Φ_n^m the monthly basis, η_s the free surface averaged over the eight months of the simulation, and η_s^m the monthly averaged free surface.

Translating a u_n modal amplitude on the monthly basis is then performed as follows:

$$u_n^m = \sum_k u_k P_{nk}, \tag{2}$$

and a vertical mode Φ_n^m is computed as follows:

$$\Phi_n^m = \sum_k \Phi_k P_{nk}^{-1}. \tag{3}$$

To better understand the importance of the basis definition, Figure 9 shows the energy transfer term between mode 1 and 3 induced by the stratification perturbation, N_{13}, in the Gulf Stream domain averaged over the month of October. When simulation averaged bases are used, the order of magnitude of the horizontal density of this term is 10^{-5} W m kg^{-1}, the same as the order of magnitude of the horizontal density for A_{12} in the same area, visible in figure 8. However, the importance of the stratification coupling collapses when monthly bases are considered: in this case, the horizontal density for N_{13} is only 10^{-7} W m kg^{-1}. Moreover, performing the computation of the advection energy transfer from mode 1 to mode 2 on the monthly bases over the Gulf Stream domain increases it by approximately $0.2 \cdot 10^9$ W compared to the same energy transfer computed using the eight months averaged basis (*c.f.* Figure 9, panel c). This accounts for a multiplication by two of A_{12} during some periods, like the end of August-beginning of September.

Since the stratification term that describes spurious energy transfer vanishes when monthly bases are used while others couplings are significantly impacted, the use of monthly bases is strongly recommended. Using an eight months averaged basis would make N_{mn} as important as the advection induced energy transfer. This also demonstrates that this term is induced by the inadequacy of the eight months averaged basis to represent instantaneous energy transfers. Using bases defined with a shorter temporal average of stratification profile $N(z)$ would be even more accurate. However, the improvement gained with monthly basis is satisfactory and is a good compromise between accuracy and computational cost induced by the multiplication of transition matrices and bases.

2 Discrete formulation of the vertical velocity

In order to better minimise numerical errors, the vertical velocity amplitude w_m is computed following the discrete formulation used in NEMO. This has been found to significantly reduce the residual of the CSW buoyancy equation (10b) (not shown here).

Following the notations of Madec & the NEMO team (2008), the continuity equation (2d) is discretised as follows:

$$\frac{1}{e_{1t}e_{2t}e_{3t}}(\delta_x^t(e_{2u}e_{3u}u) + \delta_y^t(e_{1v}e_{3v}v)) + \frac{1}{e_{3t}}\delta_z^t w = 0. \tag{4}$$

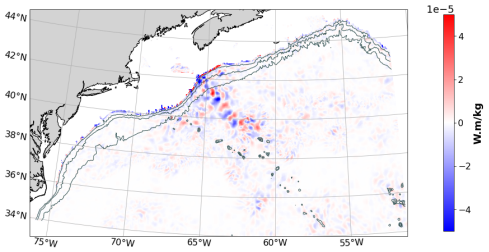

(a) Energy flux divergence

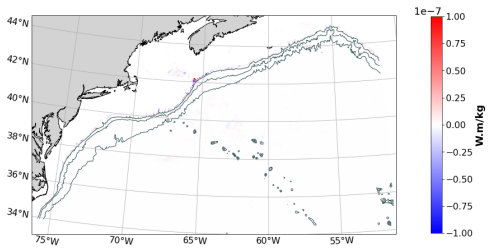

(b) Energy budget residual

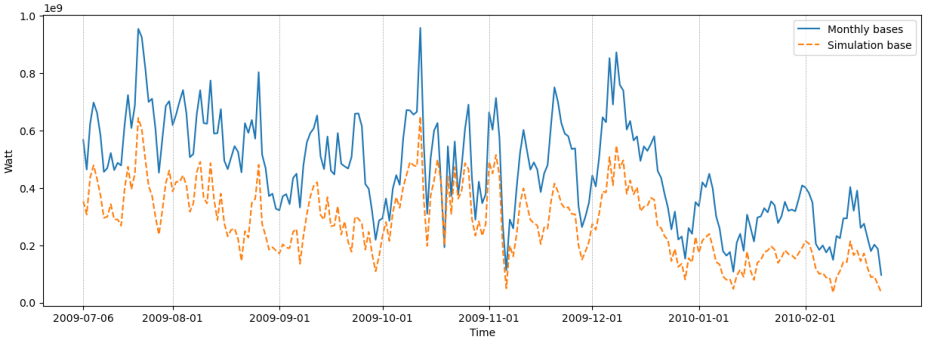

(c) Advection induced energy flux A_{mn} between mode 1 and mode 2, Gulf Stream domain

Figure 9: Top: Variable stratification coupling term N_{mn} between mode 1 and mode 3 averaged over October in the Gulf Stream domain. On panel a, the term has been computed using the eight months basis using a stratification averaged over the eight months of eNATL60. On panel b, it was computed using the basis using the monthly averaged stratification. In dark gray: isobath at 1000, 2000 and 3000 metres. Panel c: eight months temporal series of the advection induced energy flux between mode 1 and mode 2. A positive value indicates a transfer from mode 1 to mode 2. Solid blue line: coupling computed on the monthly basis. Orange dashed line: coupling computed on the simulation basis.

Here, e_{1t}, e_{2u}... refer to the horizontal metrics of the C-grid: 1, 2 and 3 denote the x, y and z axis respectively and u, v, w or t denote the grid associated with u, v, w or p. Finally, the discrete derivative of a variable X^u defined on the U grid along an axis x is noted $\delta_x^t(X^u)$ and places the variable X on the T grid – and similarly for the other grids and coordinates.

The equation (4) is then projected on the mode Φ_m^t and u, v, w are expanded on their respective modal basis $\Phi_n^u, \Phi_n^v, \varphi_n^w$. The result of this operation gives:

$$\begin{aligned}&\sum_{e_{3t}} \frac{1}{e_{1t}e_{2t}e_{3t}} \left(\delta_x^t \left(e_{2u}e_{3u} \sum_n u_n^u \Phi_n^u \right) + \delta_y^t \left(e_{1v}e_{3v} \sum_n v_n^v \Phi_n^v \right) \right) \Phi_m^t e_{3t} \\ &+ \sum_{e_{3t}} \frac{1}{e_{3t}} \delta_z^t \left(\sum_n w_n^t \varphi_n^w \right) \Phi_m^t e_{3t} = 0,\end{aligned} \tag{5}$$

where $\sum_{e_{3t}}$ indicates a summation on the vertical levels defined by the T grid. The use of the discrete orthogonality condition $\sum_{e_{3t}} \Phi_m^t \Phi_n^t e_{3t} = H^t$ and equation (5) then yields:

$$\sum_{e_{3t}} \frac{1}{e_{1t}e_{2t}e_{3t}} \left(\delta_x^t \left(e_{2u}e_{3u} \sum_n u_n^u \Phi_n^u \right) + \delta_y^t \left(e_{1v}e_{3v} \sum_n v_n^v \Phi_n^v \right) \right) \Phi_m^t e_{3t} + H^t w_n^t = 0. \tag{6}$$

Finally, with the help of $\delta_u(f^t g^t) = \overline{f^t}^u \delta_u g^t + \overline{g^t}^u \delta_u f^t$, where the bar indicates horizontal interpolation (note that $\Phi_n^t \neq \overline{\Phi_n^u}^t$), the discrete form of the continuity equation used to compute w is obtained:

$$\begin{aligned}H^t w_m^t = -\frac{1}{e_{1t}e_{2t}} \big[&H^t \delta_x^t(e_{2u}u_m^u) + H^t \delta_y^t(e_{1v}v_m^v) \\ &+ \sum_n \overline{(e_{2u}u_n^u)}^t \sum_{e_{3t}} \delta_x^t(e_{3u}\Phi_n^u)\Phi_m^t + \sum_n \overline{(e_{1v}v_n^v)}^t \sum_{e_{3t}} \delta_x^t(e_{3v}\Phi_n^v)\Phi_m^t \\ + \sum_n \delta_x^t(e_{2u}u_n^u) \sum_{e_{3t}} (\overline{e_{3u}\Phi_n^u}^t - e_{3t}\Phi_n^t)\Phi_m^t &+ \sum_n \delta_y^t(e_{1v}v_n^v) \sum_{e_{3t}} (\overline{e_{3v}\Phi_{vn}^v}^t - e_{3t}\Phi_n^t)\Phi_m^t \big].\end{aligned} \tag{7}$$

3 Compensation between vertical shear and buoyancy induced energy transfers

As can be seen in Figure 3 (panels c and d) or in Figure 5(a) in the Gulf Stream domain, a compensation between the vertical mesoscale shear induced energy flux $\sum_j V_{1j}$ and the background buoyancy gradient flux $\sum_j B_{1j}^{os}$ seems to occur in part of the North Atlantic. This section aims at explaining analytically this compensation based on an idealistic configuration. This allows us to provide conditions where this compensation is likely to occur.

To this aim, we consider two internal tide modes n and m propagating in specific directions and encountering an unidirectional jet in thermal wind balance. This configuration is usually found near generation sites where the internal tide beam propagates in a well defined direction. One example in the eNATL60 domain is located offshore of the US East coast generation site, where the internal tide beam encounters the Gulf Stream. The current $\boldsymbol{U} = U\boldsymbol{e}_x$ is chosen to flow along the x direction and the horizontal gradient of buoyancy $\boldsymbol{\nabla}_h(B)$ is orthogonal to $\boldsymbol{U}$ and directed along the y direction (note that, on the f-plane, the problem considered is invariant by horizontal rotation).

In this situation, the thermal wind relationship gives:

$$\partial_z U = -\frac{1}{f} \partial_y B.$$

Two plane waves associated with possibly different vertical modes n and m are considered:

$$(u_n, v_n, w_n, p_n) = (\hat{u}_n, \hat{v}_n, \hat{w}_n, \hat{p}_n) e^{i(\omega t - k_n cos\theta_n x - k_n sin\theta_n y)},$$
$$(u_m, v_m, w_m, p_m) = (\hat{u}_m, \hat{v}_m, \hat{w}_m, \hat{p}_m) e^{i(\omega t - k_m cos\theta_m x - k_m sin\theta_m y)},$$

with k_j the wave vector modulus of the mode j and θ_j the angle between the corresponding wavevector $\boldsymbol{k}_j$ and $\boldsymbol{e}_x$. These waves obey the following relations obtained from the coupled shallow water equations (10) in the absence of a background flow, topography and horizontal variations of stratification:

$$\hat{p}_j = \hat{w}_j \frac{c_j^2}{i\omega}, \tag{8}$$
$$\hat{u}_j = \frac{i\omega \sin\theta_j + f\cos\theta_j}{f\sin\theta_j - i\omega\cos\theta_j} \hat{v}_j. \tag{9}$$

With the thermal wind hypothesis, the buoyancy and vertical shear induced energy fluxes (see eq. 11) become:

$$V_{mn} = 2Re\left(\frac{w_n}{f} u_m^* B_{y,nm}\right),$$
$$B_{mn}^{os} = 2Re\left(\frac{p_m^*}{c_m^2} v_n B_{y,mn}\right),$$

with $B_{y,mn} = \int_{-H}^{\overline{\eta}} \partial_y B \varphi_m \Phi_n dz$, and $\cdot^*$ denoting the complex-conjugate. By using the polarisation relation (8) to substitute the pressure amplitude p_j by w_j, and u_j^* by v_j^*, we obtain for the symmetric contribution of the vertical shear and buoyancy gradient energy transfer terms:

$$\begin{aligned} V_{mn} + V_{nm} + B_{mn}^{os} + B_{nm}^{os} =& 2Re(B_{y,nm} w_n v_m^* (\frac{i\omega\cos\theta_m + f\sin\theta_m}{-i\omega\sin\theta_m - f\cos\theta_m} - \frac{f}{i\omega}) \\ &+ B_{y,mn} w_m^* v_n (\frac{i\omega\cos\theta_n + f\sin\theta_n}{-i\omega\sin\theta_n - f\cos\theta_n} - \frac{f}{i\omega})). \end{aligned}$$

From this expression we see that there is compensation (*i.e.* the above expression vanishes) if the following condition holds:

$$\cos\theta_j (f^2 - \omega^2) = 0, \tag{10}$$

with $j = m$, or n. This condition is verified in the case of two waves propagating perpendicularly to the mesoscale current, or near critical latitude where $\omega = f$. In the latter case, the compensation is independent of the waves orientation.

Open Research Section

Data from the NEMO ENATL60 simulation can be accessed at `https://zenodo.org/record/4032732` and `https://github.com/ocean-next/eNATL60/blob/master/05_data.md`. The scripts used for the analysis presented in the paper can be accessed at `https://github.com/NoeLahaye/ITideNATL` and `https://gitlab.inria.fr/abella/bella_et_al_2024`.

Acknowledgments

A. Bella is partially funded by Région Bretagne through the ARED PhD funding program (COMIOE project 15995). This research received support from the French research funding agency (ANR) under the ModITO project (ANR-22-CE01-0006-01), and from the CNES through the project DIEGO.

References

Alford, M. H., Simmons, H. L., Marques, O. B., & Girton, J. B. (2019). Internal tide attenuation in the north pacific. *Geophysical Research Letters*, *46*, 8205–8213. doi: 10.1029/2019GL082648

Ansong, J. K., Arbic, B. K., Alford, M. H., Buijsman, M. C., Shriver, J. F., Zhao, Z., ... Zamudio, L. (2017). Semidiurnal internal tide energy fluxes and their variability in a global ocean model and moored observations. *Geophys. Res. Oceans*, *122*, 1882–1900. doi: 10.1002/2016JC012184

Arbic, B. K., Richman, J. G., Shriver, J. F., Timko, P. G., Metzger, E., & Wallcraft, A. J. (2012). Global modeling of internal tides within an eddying ocean general circulation model. *Oceanography*, *Volume 25(2)*, 20-29. doi: 10.5670/oceanog.2012.38

Arbic, B. K., Wallcraft, A., & Metzger, E. (2010). Concurrent simulation of the eddying general circulation and tides in a global ocean model. *Ocean Modelling*, *32*, 175–187. doi: 10.1175/10.1016/j.ocemod.2010.01.007

Ballarotta, M., Ubelmann, C., Pujol, M.-I., Taburet, G., Fournier, F., Legeais, J.-F., ... Picot, N. (2019). On the resolutions of ocean altimetry maps. *Ocean science*, 1091–1109.

Barbot, S., Lyard, F., Tchilibou, M., & Carrere, L. (2021, November). Background stratification impacts on internal tide generation and abyssal propagation in the western equatorial Atlantic and the Bay of Biscay. *Ocean Sci.*, *17*(6), 1563–1583. doi: 10.5194/os-17-1563-2021

Bella, A., Lahaye, N., & Tissot, G. (2023). Internal tides energy transfers and interactions with the mesoscale circulation in two contrasted areas of the north atlantic. *Mathematics of Planet Earth, Stochastic Transport in Upper Ocean dyamics II*, *11*. doi: 10.1007/978-3-031-40094-0_1

Brodeau, L., Le Sommer, J., & Albert, A. (2020, September). *Ocean-next/eNATL60: Material describing the set-up and the assessment of NEMO-eNATL60 simulations.* Zenodo.

Buijsman, M. C., Stephenson, G. R., Ansong, J. K., Arbic, B. K., Mattias Green, J. A., Richman, J. G., ... Zhao, Z. (2020). On the interplay between horizontal resolution and wave drag and their effect on tidal baroclinic mode waves in realistic global ocean simulations. *Ocean Modelling*, *152*. doi: 10.1016/j.ocemod.2020.101656

de Lavergne, C., Falahat, S., Madec, G., Roquet, F., Nycander, J., & Vic, C. (2019). Toward global maps of internal tide energy sinks. *Ocean Modelling*, *137*, 52–75. doi: 10.1016/j.ocemod.2019.03.010

de Lavergne, C., Vic, C., Madec, G., Roquet, F., Waterhouse, A. F., Whalen, C. B., ... Hibiya, T. (2020). A parameterization of local and remote tidal mixing. *Journal of Advances in Modeling Earth Systems*, *12*. doi: 10.1029/2020MS002065

Duda, T. F., Lin, Y.-T., Buijsman, M. C., & Newhall, A. E. (2018). Internal tidal modal ray refraction and energy ducting in baroclinic gulf stream currents. *Journal of Physical Oceanography*, *48*, 1969–1993. doi: 10.1175/JPO-D-18-0031.1

Dunphy, M., & Lamb, K. G. (2014). Focusing and vertical mode scattering of the first mode internal tide by mesoscale eddy interaction. *Journal of Geophysical Research: Oceans*, *33*, 523–536. doi: 10.1002/2013JC009293

Gerkema, T. (2016). *An introduction to tides.* Yerseke: Royal NIOZ.

Kelly, S. M. (2016). The vertical mode decomposition of surface and internal tides in the presence of a free surface and arbitrary topography. *Journal of Physical Oceanography*, *Volume 46, Issue 12*, 3777-3788. doi: 10.1175/JPO-D-16-0131.1

Kelly, S. M., Lemursiaux, P. F. J., Duda, T. F., & JR., P. J. H. (2016). A coupled-mode shallow-water model for tidal analysis: Internal tide reflection and refraction by the gulf stream. *Journal of Physical Oceanography*, *46*, 3661–3679. doi: 10.1175/JPO-D-16-0018.1

Kelly, S. M., & Lermusiaux, P. F. J. (2016). Internal-tide interactions with the gulf stream and middle atlantic bight shelfbreak front,. *Journal of Geophysical Research: Oceans*, *121*, 6271–6294. doi: 0.1002/2016JC011639

Lahaye, N., Gula, J., & Roullet, G. (2020). Internal tide cycle and topographic scattering over the north mid-atlantic ridge. *Journal of Geophysical Research: Oceans*, *125*, e2020JC016376. https://doi. org/10.1029/2020JC016376.

Löb, J., Köhler, J., Mertens, C., Walter, M., Li, Z., & von Storch, J. S. (2020). Observations of the low-mode internal tide and its interaction with mesoscale flow south of the azores. *Journal of Geophysical Research: Oceans*, *125*. doi: 10.1029/2019JC015879

Madec, G., & the NEMO team, N. o. e. (2008). *Note du pôle de modélisation.* No 27, ISSN No 1288-1619.: Institut Pierre-Simon Laplace (IPSL), France.

Munk, W., & Wunsch, C. (1998). Abyssal recipes ii: energetics of tidal and wind mixing. *Deep-Sea Research*, *Volume 45, Issue 12*, 1977-2010. doi: 10.1016/S0967-0637(98)00070-3

Pan, Y., Haley, P. J., & Lermusiaux, P. F. J. (2021). Interactions of internal tides with a heterogeneous and rotational ocean. *Journal of Fluid Mechanics*, *920*. doi: 10.1017/jfm.2021.423

Pickering, A., Alford, M., Nash, J., Rainville, L., Buisjman, M., Shan Ko, D., & Lim, B. (2015). Structure and variability of internal tides in luzon strait. *Journal of Physical Oceanography*, *45*, 1574-1594. doi: 10.1175/JPO-D-14-0250.1

Ponte, A. L., & Klein, P. (2015). Incoherent signature of internal tides on sea level in idealized numerical simulations. *Geophysical Research Letters*, *Volume 42*, 1520–1526. doi: 10.1002/2014GL062583

Rainville, L., & Pinkel, R. (2005). Propagation of low-mode internal waves through the ocean. *Journal of Physical Oceanography*, *36*, 1220-1236.

Savage, A. C., Waterhouse, A. F., & Kelly, S. M. (2020). Internal tide nonstationarity and wave–mesoscale interactions in the tasman sea. *Journal of Physical Oceanography*, *50*, 2931 - 2951. doi: 10.1175/JPO-D-19-0283.1

Shriver, J. F., G., R. J., & K., A. B. (2014). How stationary are the internal tides in a high-resolution global ocean circulation model? *J. Geophys. Res. Oceans*, *Volume 119*, 2769–2787. doi: 10.1002/2013JC009423

Tchilibou, M., Koch-Larrouy, A., Barbot, S., Lyard, F., Morel, Y., Jouanno, J., & Morrow, R. (2022). Internal tides off the amazon shelf during two contrasted seasons: Interactions with background circulation and ssh imprints. *Ocean Science*. doi: 10.5194/os-2021-114

Vic, C., Garabato, A. C. N., Green, J. A. M., Waterhose, A. F., Zhao, Z., Melet, A., ... Stephenson, G. R. (2019). Deep-ocean mixing driven by small-scale internal tides. *Nature communications*. doi: 10.1038/s41467-019-10149-5

Whalen, C. B., de Lavergne, C., Naveira Garabato, A. C., Klymak, J. M., MacKinnon, J. A., & Sheen, K. L. (2020). Internal wave-driven mixing: governing processes and consequences for climate. *Nature Reviews, Earth & Environment*. doi: 10.1038/s43017-020-0097-z

Zaron, E. D., Musgrave, R. C., & Egbert, G. D. (2022). Baroclinic tidal energetics inferred from satellite altimetry. *Journal of Physical Oceanography*, 1015–1032. doi: 10.1175/JPO-D-21-0096.1

Zhao, Z. (2018). The global mode-2 m2 internal tide. *Journal of Geophysical Research: Oceans*, *Volume 123*, 7725–7746. doi: 10.1029/2018JC014475